frontiers in Materials

ORIGINAL RESEARCH
published: 30 July 2020
doi: 10.3389/fmats.2020.00244

Corrosion Behavior of an Equiatomic CoCrFeMnNi High-Entropy Alloy- a Comparison Between Selective Laser Melting and Cast

Haoping Peng[1], Zehuan Lin[2], Ruidi Li[2,3], Pengda Niu[2] and Zhijian Zhang[2]*

[1] Jiangsu Key Laboratory of Oil-Gas Storage and Transportation Technology, Changzhou University, Jiangsu, China, [2] State Key Laboratory of Powder Metallurgy, Central South University, Changsha, China, [3] Shenzhen Institute of Central South University, Shenzhen, China

The corrosion behaviors of equiatomic CoCrFeMnNi high-entropy alloys (HEAs) were comparatively investigated between selective laser melting (SLM) and casting. The cast sample shows better corrosion resistance in 3.5 wt.% NaCl solution than the SLM printed sample due to the higher density of dislocations, pores, and cracks in SLM samples, which significantly reduces their corrosion resistance. Furthermore, it is found that the corrosion resistance is different between the planes parallel and perpendicular to the building direction of SLM sample because of the differences in grain orientation, grain size, and surface morphology. Electrochemical anode dissolution rates of the SLM printed CoCrFeMnNi HEAs on their planes parallel and perpendicular to the building direction are calculated and the results show that the pores and cracks dominate the corrosion resistance rather than the grain boundary and the grain orientation.

Keywords: high-entropy alloys, corrosion resistance, selective laser melting, equiatomic CoCrFeMnNi, casting

OPEN ACCESS

Edited by:
Lai-Chang Zhang,
Edith Cowan University, Australia

Reviewed by:
Liang-Yu Chen,
Jiangsu University of Science and Technology, China
Yang Yang,
Guangdong University of Technology, China

****Correspondence:***
Haoping Peng
penghp@cczu.edu.cn

Specialty section:
This article was submitted to Structural Materials, a section of the journal Frontiers in Materials

Received: *21 May 2020*
Accepted: *03 July 2020*
Published: *30 July 2020*

Citation:
Peng H, Lin Z, Li R, Niu P and Zhang Z (2020) Corrosion Behavior of an Equiatomic CoCrFeMnNi High-Entropy Alloy- a Comparison Between Selective Laser Melting and Cast. Front. Mater. 7:244. doi: 10.3389/fmats.2020.00244

INTRODUCTION

High entropy alloys (HEAs) consist of five or more metallic elements with equimolar or near-equimolar ratios, which feature satisfying properties, such as excellent mechanical properties, predominant corrosion resistance, magnetism and high resistivity (Ye et al., 2016). In the past decade, HEAs have attracted considerable attention because of their excellent properties which can be tailored by adjusting the chemical compositions (Zhang et al., 2014b).

Selective laser melting (SLM), as one of the additive manufacturing (AM) method, can produce a three-dimensional model with highly complex geometric features and ultrafine microstructure (Joseph et al., 2017; Li L. et al., 2020; Li R. et al., 2020; Niu et al., 2020). Compared to the traditional casting and forging process, SLM has many advantages such as the simplified manufacturing procedures and the capacity of fabricating parts with high geometry complexity (Chen et al., 2017). Besides, the SLM-produced metallic parts have a more homogenized microstructure and better properties because of its high solidification rate (10^5 Ks^{-1}) (Niu et al., 2019). Based on the advantages of the SLM, several HEAs with excellent properties were fabricated through SLM. For instance, SLM printed equimolar AlCoCrFeNi HEA shows higher micro-hardness of 632.8 HV than that of the casted and the electron beam melting printed samples (Brandl et al., 2012). Zhang et al. (2018) studied the thermal-mechanical behavior of a SLM produced WTaMoNb refractory HEA, which also exhibits better properties than its casted counterparts. SLM is layer-wise processing

that fabricates layer-by-layer structure in printed metallic parts (Montero Sistiaga et al., 2016), which implies that their microstructure, mechanical and chemical properties in the planes parallel and perpendicular to the building direction are quite different. Our previous work studied the crystal morphology of SLM printed CoCrFeMnNi HEA in the planes parallel and perpendicular to the building direction and concluded that there are elongated columnar grains in the parallel plane, while equiaxed grains exist in the perpendicular plane (Li R. et al., 2018). Wysocki et al. (2017) reported significant differences between the planes parallel and perpendicular to the building direction of the SLM printed CP-Ti in the mechanical properties and microstructure. Kong et al. (2019) reported that the grain size of the SLM printed 316L stainless steel in the planes parallel to the building direction is smaller than that in the perpendicular planes, and many low-angle boundaries formed in the perpendicular planes, which results in the lower elongation in perpendicular planes compared to that of the parallel planes. As for the corrosion behavior, Zhang et al. (2019) found that the planes perpendicular to the building direction of the TiC/Inconel 718 composite fabricated by SLM have superior corrosion resistance in 3.5 wt.% NaCl solution. Chen et al. (2018) demonstrated that the planes parallel to the building direction of the SLM printed Al-12Si alloy exhibited better corrosion property compared to that of the planes perpendicular to the building direction in the 3.5 wt.% NaCl solution. Therefore, in most cases, the corrosion resistance between planes parallel and perpendicular to the building direction is different because of the difference in texture and grain morphology.

Recently, the corrosion behaviors of some HEAs in the aqueous solution have been reported. Luo et al. (2018) compared the corrosion behavior of casted CoCrFeMnNi HEA with that of 304L stainless steel in 0.1 M H_2SO_4 solution and reported that the lower anti-corrosion performance of the HEA resulted from the low contents of Cr and the extensive formation of metal hydroxide in the passive film. N. Kumar et al. (2017) investigated the corrosion behavior of casted $Al_{0.1}$CoCrFeNi HEA in the 3.5 wt.% NaCl solution and reported that the general corrosion resistance and pitting potential of the HEA was better than that of the 304L stainless steel because its Cr contents in HEA is higher than that of the 304L stainless steel. Rodriguez et al. (Ziomek.-Moroz et al., 2017) studied the corrosion behavior of the CoCrFeMnNi HEAs in acidic sodium chloride solution with CO_2 and claimed that the Cr contents can significantly affect the corrosion rate of the HEAs.

Numerous studies have been conducted on the SLM printed CoCrFeMnNi alloy. Our previous study also detailed investigated the processability, non-equilibrium microstructure, and mechanical properties of the CoCrFeMnNi alloy (Li R. et al., 2018). However, unlike mechanical properties, corrosion behaviors of SLM printed CoCrFeMnNi alloy were rarely discussed in recent studies. SLM printed products CoCrFeMnNi can be used in a wider range, such as pumps and valves in fluid systems. The wide application of SLM products must have certain requirements for its corrosion performance. Therefore, the research on the corrosion performance of SLM produced CoCrFeMnNi becomes very important. Today, the SLM produced CoCrFeMnNi HEA has been successfully prepared, but its corrosion performance has not been studied. Understanding its corrosion behavior is necessary on the purpose to promote the application of CoCrFeMnNi alloy as corrosion resistance is an important indicator of a material that needs to be considered during its service as pumps and valves. In this paper, the corrosion behaviors of different planes of the SLM printed CoCrFeMnNi HEA were investigated in the 3.5 wt.% NaCl solution, which was compared with its casting counterparts. This paper systematically studied the corrosion behavior of CoCrFeMnNi HEA alloys between traditional casting and SLM.

EXPERIMENTAL PROCEDURES

Sample and Solution Preparation

The size of the equiatomic CoCrFeMnNi samples produced by SLM and cast is 10 mm × 10 mm × 10 mm. HEA powder used in this study is the same powder in our previous work (Li R. et al., 2018), which was produced by the gas atomization method under an argon atmosphere and the powder particle size distribution ranges from 5 to 45 μm with a median particle diameter of 36 μm. The impurities in the atomized powder are Si below 0.001 at.%, oxygen below 0.0032 at.%, carbon below 0.0002 at.%, and sulfur below 0.00025 at.%. The oxygen content is below 0.3 vol.% during printing. The relative densities of printed samples are 98.2%. The SLM samples were manufactured by the FS271 M machine (Farsoon, Inc., China) equipped with a 500 W fiber laser. The scanning parameters are scanning speed of 800 mm/s, laser power of 400 W, scan interval of 0.09 mm, and layer thickness of 0.03 mm. The SLM experiments were performed under an argon atmosphere. The building substrate was a steel plate. During printing, the samples are scanned with long vectors and the direction of scanning is kept at 67° angle rotation between each layer. The rest of the scanning parameters are the most optimized parameters in our last work (Li R. et al., 2018). The casted samples were produced in a vacuum induction furnace with high purity metal. The ingot was hot rolled to 50% thickness at 1000 ℃, homogenized at 1300 ℃ for 3 h under an argon atmosphere, and subsequently water-quenched. The printed and casted samples consist of nearly full of single FCC phase according to the XRD analysis.

In this paper, planes perpendicular to the building direction are named as XY planes while planes parallel to building direction are named as XZ planes. The corrosion samples were cut from the XY and XZ planes of the SLM printed and casted HEA samples with the same size of 10 mm × 10 mm × 2 mm. Copper wires were attached to the back of all samples by conducting resin and were covered by epoxy resin. Then, the samples' surfaces were ground and polished using standard metallographic procedures.

Weight Loss Test

The weight loss test was conducted in the 3.5 wt.% NaCl solution. Specimens with a size of 10 mm × 10 mm × 1 mm cut from the HEA samples are prepared. The back and side of the sheets were coated with the resin to ensure that the front side was the only face exposed to the corrosion solution. Afterward, these

samples were labeled and their initial weights were measured by the analytical balance with an accuracy of 0.1 mg. Tested samples were taken out, respectively from the solution simultaneously after immersing for 3, 6, 9, 12, 15, and 18 days. In the light of standard ISO 8407-1991, the surfaces of the immersed sample were cleaned by nitric acid for 5 min in the room temperature, dried in the air, and weighed by the immersed solution. Due to the absorption of the resin in the 3.5 wt.% NaCl solution, a blank sample was prepared and immersed in the NaCl solution. The weight loss rate ($g{\cdot}m^{-2}{\cdot}h^{-1}$) was calculated in Eq. (1) (Chen et al., 2018):

$$v = [(w_1 - w_2 + \Delta w) - (m_1 - m_2)]/(s{*}t) \quad (1)$$

where w_1 and w_2 are the weight of the samples before and after immersion in 3.5 wt.% NaCl solution, Δw the weight of the resin absorbed water, m_1 and m_2 the weight of background sheets with and without clean in the nitric acid, respectively, s the exposed area of the sheets (m^2), and t the immersion time (h).

Electrochemical Measurements

The electrochemical measurements were performed in the 3.5 wt.% NaCl solution using an electrochemical workstation (CHI 760E, Huachen, China) at room temperature. A three-electrode cell system was used in the electrochemical tests. A platinum plate was used as the counter electrode, a saturated calomel electrode (SCE) was used as the reference electrode and the HEAs samples were used as the working electrode in the system. Before the Tafel curves tests and electrochemical impedance spectroscopy (EIS) measurements, the samples were immersed in the 3.5 wt.% NaCl solution for 30 min to get a stable open circuit potential (OCP). The Tafel curves were recorded from the −0.25 V to + 0.25 V referring to OCP with a scan rate of 0.01 V/s and sensitivity of 10^{-3} A/V. The electrochemical impedance spectroscopy (EIS) measurements were measured at the initial voltage of OCP, scanning from the 0.01 Hz to 10^5 Hz at a sensitivity of 5×10^{-3} V.

All samples were tested three times to ensure data accuracy. The data from the electrochemical measurements were fit by a software named Nova 2.1.

Characterization

The microstructures of the HEAs samples after polishing, weight loss test and the electrochemical measurements were characterized by scanning electron microscopy (SEM, QuantaFEG250, American).

RESULTS

Weight Loss Test

The relationships between the weight loss rates and immersion time of the different planes in SLM printed and casted HEAs in the 3.5 wt.% NaCl solution are exhibited in **Figure 1**. It is obvious that the curves of the three samples have a similar tendency. The weight loss rate decreased quickly in the initial period stage of the corrosion test. This phenomenon can be explained as the solution corroded the loose surface structure (Guo et al., 2012). By contrast, all of the curves feature flat fluctuation after 6 days of immersion. It indicates that the corrosion products and dense oxide layers are formed after the surface corrosion (Gu et al., 2012), which reduces the weight loss rate. At the beginning of the corrosion test, XZ-plane shows the highest weight loss rate, which suggests that the XZ-plane loses more mass in the experiment.

The microscopic images of oxide films of CoCrFeMnNi alloy produced by the different forming processes are shown in **Figure 2**. As seen from **Figures 2a,d**, the oxidation film of the XZ-plane is coarse and discontinuous, while the XY-plane and planes of the casted CoCrFeMnNi alloy are relatively dense and continuous (**Figures 2b,c,e,f**). This indicates that in the process of soaking in solution, the oxidation film formed in the XY-plane of SLM printed CoCrFeMnNi alloy while cast-CoCrFeMnNi alloy has a higher resistance to chloride ion corrosion, which can be proved by comparing the concentration of chlorine ions on the oxidation film from the EDS (**Figures 2g–i**). It could be seen that the chemical compositions in the surface of the casted CoCrFeMnNi alloy have no obvious changes except for the contents of oxygen, which is because the oxidation film is denser and smoother.

Electrochemical Studies

Figure 3 shows the Tafel curves of the XY plane, XZ plane of the printed CoCrFeMnNi, and plane of the casted CoCrFeMnNi, respectively. The corrosion potential (E_{corr}) and corrosion current density (i_{corr}) are obtained by linear fitting of the Tafel curves and are listed in **Table 1**. The E_{corr} and i_{corr} values of different planes are significantly different. The corrosion potential of XY plane of the printed CoCrFeMnNi is the highest [−0.34622 V (vs. SCE)], followed by its XZ plane [−0.32279 V (vs. SCE)] and that of the casted CoCrFeMnNi is the lowest [−0.26355 V (vs. SCE)]. As for corrosion current density, the casted CoCrFeMnNi has the lowest value (1.1983×10^{-7} A/cm^2), while that of the XY plane has middle value (1.2317×10^{-7} A/cm^2) and that of XZ plane has the highest value (1.3295×10^{-7} A/cm^2). In general, both of the XY and XZ planes of the printed CoCrFeMnNi and its casted counterpart exhibit much lower i_{corr} values compared with many reported HEAs such as $CuCr_2Fe_2Ni_2Mn_2$ (2.33×10^{-5} A/cm^2) (Ren et al., 2012), AlMgZnSnPbCuMnNi (2.93×10^{-5} A/cm^2) (Gan et al., 2013), AlCrFeCuCo (6.67×10^{-6} A/cm^2) (Qiu et al., 2013), $FeCoNiCrCu_{0.5}$ (7.23×10^{-7} A/cm^2) (Hsu et al., 2005), $Al_{25}Ti_{25}Ga_{25}Be_{25}$ (2.62×10^{-6} A/cm^2) (Fazakas et al., 2014), and $Al_{0.9}CoCrFeNiTi_{0.5}$ (3.10×10^{-7} A/cm^2) (Qiu et al., 2019), which indicates extraordinarily better corrosion resistance of the equiatomic CoCrFeMnNi HEA.

Based on electrochemical corrosion theory, E_{corr} is a thermodynamic parameter and i_{corr} is a kinetic parameter. The relation between the corrosion current density and the corrosion rates of the samples can be given as: (Zhang et al., 2014a):

$$v = {Mi_{corr}}/{nF}\ \frac{Mi_{corr}}{nF} \quad (2)$$

where v is the corrosion rate, n the valence of the metal, F the Faraday constant, M the molar mass of the metal, and i_{corr}

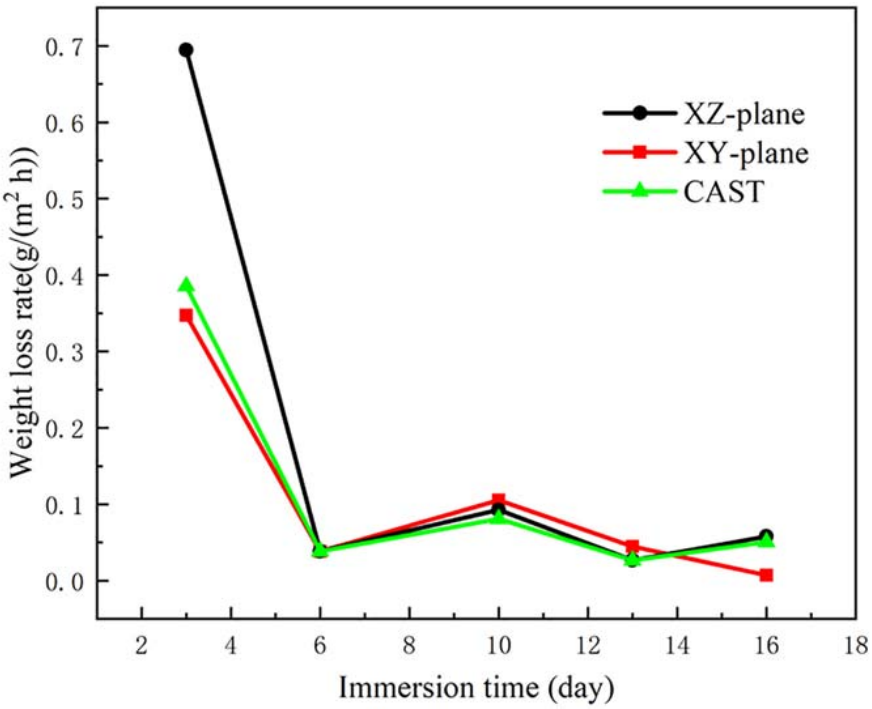

FIGURE 1 | Weight loss rate of the SLM printed HEA alloy on the XY and XZ planes and casted HEA after immersing in the aerated 3.5 wt.% NaCl solution at room temperature.

the corrosion current density. From the formula, the corrosion current density is the main factor affecting the corrosion rate compared to the corrosion potential. Therefore, the casted CoCrFeMnNi samples has the best corrosion resistance compared to that of the XY and XZ planes of the printed samples.

Figures 4A–C show the representative Nyquist and bode plots of the XY and XZ planes of the SLM printed and casted CoCrFeMnNi HEAs immersed in the 3.5 wt.% NaCl solution. The electrochemical impedance test data fitted by the electrical equivalent circuit (EEC) are inserted in **Figure 4D**.

In **Figure 4A**, the Nyquist plotted curves of the three HEA samples have similar characteristics where capacitive semicircles cover the all-frequency region. The diameters of the capacitive semicircle of the casted HEA are higher than that of the SLM printed HEA, which implies that the corrosion resistance of the casted HEA is better than that of the SLM printed HEA in the 3.5 wt.% NaCl solution (Della Rovere et al., 2012). The bode plots of the printed and casted samples are also provided. From **Figure 4B**, the relationships between log | Z| and log |Z| are observed in the frequency ranging from 10^{-2} Hz to 10^{5}Hz. All of the three samples have their maximal phase angle below 90°, which indicates that these samples feature pseudocapacitance in the tests (Luo et al., 2018). During the corrosion tests, when the frequency value equals 10^{-1}, its corresponding |Z| which is associated with the polarization resistance determines the corrosion resistance of the tested alloy (Della Rovere et al., 2012). From **Figure 4C**, the value of | Z| of the XY plane at 10^{-1} Hz is higher than that of the XZ plane of the printed HEA, while the casted HEA is the highest, which indicates that the corrosion-resistant property of the casted HEA is better than that of the SLM printed HEA.

In this experiment, the EEC model is used to fit the AC impedance test at the OCP condition (Kocijan et al., 2011). The chi-square values ($\Sigma\chi^2$) in **Table 2** are very small, which indicates that the model has a good fitting quality. According to the EEC schematic diagram in **Figure 4D**, Q_{dl} is in parallel with the polarization resistance (R_p) and subsequently in series with the solution resistance (R_e).

The EEC fitting parameters obtained from the equiatomic CoCrFeMnNi are shown in **Table 2**. The corrosion resistance of the material is evaluated by R_p, which is seriously affected by the material passive film (Fajardo et al., 2014). The casted CoCrFeMnNi has the highest R_p value. Furthermore, R_p value of the XY plane is higher than that of the XZ plane of the printed samples. This indicates that the passive film of the casted CoCrFeMnNi is more stable leading to a higher corrosion resistant performance compared to the SLM printed CoCrFeMnNi. And the corrosion resistant of the XY plane is better than that of the XZ plane (Kocijan et al., 2011). In general, for a single capacitive behavior, its corresponding n_{dl} should be higher than 1. Noticing that all the samples have their n_{dl} values lower than 1, which indicates their electrochemical behavior is not a simple capacitive behavior.

Figure 5 shows the surface morphology of the samples after electrochemical tests. It can be seen from **Figures 5a,b** that the pitting corrosion occurs along the edges of cracks and holes.

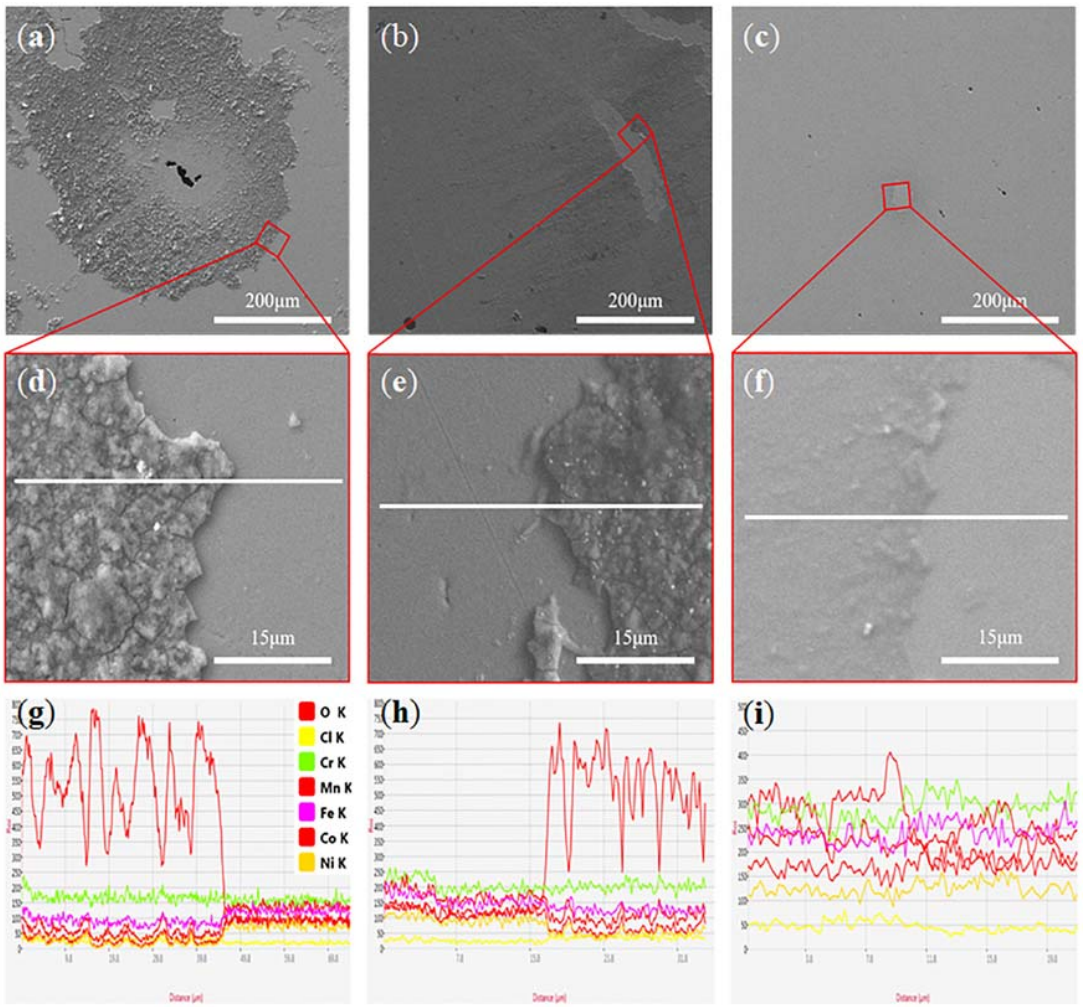

FIGURE 2 | SEM image of the Surface corrosion morphologies of samples with different processes after 14 days of immersion in 3.5 wt.% NaCl solution: **(a)** XZ plane of the SLM printed CoCrFeMnNi alloy; **(b)** XY plane of the SLM printed CoCrFeMnNi alloy; **(c)** casted CoCrFeMnNi alloy; **(d)** Oxide film boundary of the XZ plane of SLM printed CoCrFeMnNi alloy; **(e)** Oxide film boundary of the XY plane of SLM printed CoCrFeMnNi alloy; **(f)** Oxide film boundary of the casted CoCrFeMnNi alloy; **(g–i)** EDS spectra of selection areas, respectively.

For the casted CoCrFeMnNi (**Figure 5c**), the pitting corrosion usually occurs continuously at one point.

DISCUSSION

Comparison of Cast Sample and SLM Printed Sample

In this paper, the results of the electrochemical tests were used to investigate the corrosion resistance of the casted CoCrFeMnNi and the SLM-produced CoCrFeMnNi alloy on its/their XY and XZ planes. According to Tafel curves (**Figure 3**), the corrosion current density for casted CoCrFeMnNi is lower than that of the SLM produced CoCrFeMnNi. From the electrochemical impedance test (**Figure 4**), casted CoCrFeMnNi also shows better corrosion resistance than that of the SLM produced CoCrFeMnNi. Such a distinction in corrosion property of the CoCrFeMnNi prepared by different processes is induced by the different microstructure and phase compositions between them. From **Figures 2**, **5**, it is obvious that the surface of casted CoCrFeMnNi is more compact, while that of SLM produced CoCrFeMnNi is not completely dense. A certain number of pores and cracks exist on the surface of SLM produced CoCrFeMnNi samples. In the corrosion process, the structural defects increase the effective area of the corrosion and provide the passages for the corrosive ions entering into the surface film (Liu et al., 2011; Yao et al., 2011; Fan et al., 2013). In the process of surface film corrosion, pores play the role of inward diffusion while cracks play the role of transverse expansion (Dong et al., 2015). In the 3.5 wt.% NaCl solution, chloride ions tend to diffuse inward through cracks and pores (Shang et al., 2009; Pan et al., 2013). The presence of chloride ions can accelerate the rate of dissolution of the metallic element within the pores and cracks (Wang et al., 2013). As can be seen in **Figure 5**, holes and

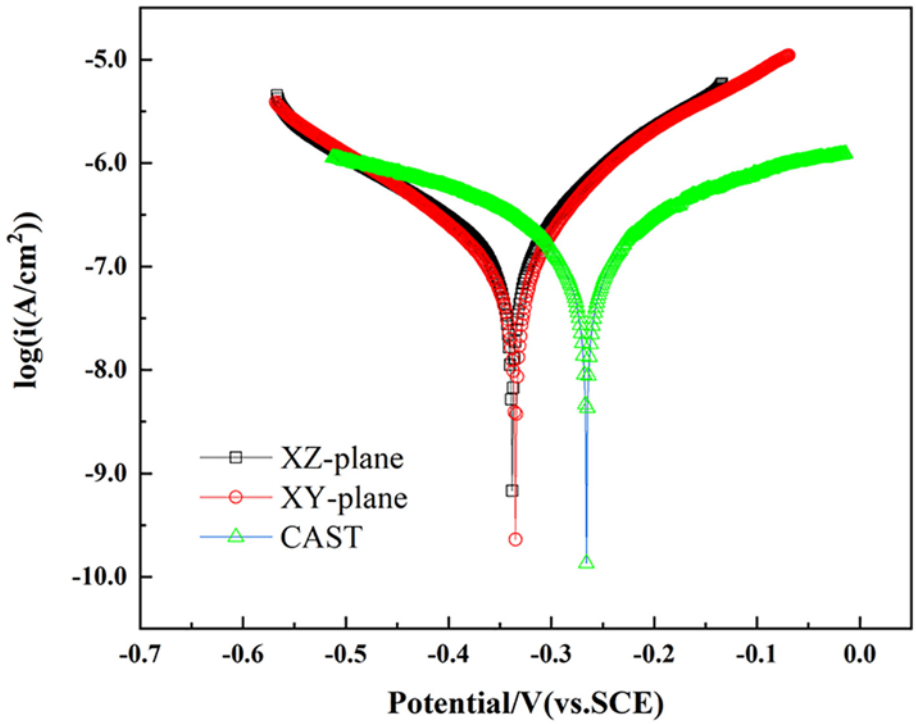

FIGURE 3 | Tafel curves of the XY and XZ planes for the SLM printed HEA and casted HEA in the aerated 3.5 wt.% NaCl solution at room temperature.

TABLE 1 | The electrochemical parameters obtained from Tafel curves of the SLM printed HEA on the XY and XZ planes and casted HEA in the aerated 3.5 wt.% NaCl solution.

Anodes	E_{corr} (vs. SCE)/V	i_{corr} (A/cm^2)
XZ plane CoCrFeMnNi	−0.32279	1.3295×10^{-7}
XY plane CoCrFeMnNi	−0.34622	1.2317×10^{-7}
Casted CoCrFeMnNi	−0.26355	1.1983×10^{-7}

i_{corr}: corrosion current density; E_{corr}: corrosion potential.

cracks in SLM produced CoCrFeMnNi provide the condition for pitting to occur around them and along their boundaries. For the casted CoCrFeMnNi, the process of pitting is producing a weak area on the smooth surface under the constant corrosion of chloride ions, and then corrosion on it to form pitting pits. This process means that the appearance of pitting on the cast sample requires more effort.

Phase composition is another important factor that affects corrosion performance. From **Figure 6**, high density of dislocations' accumulation, dislocation entanglement, bending, and phase precipitation exist in the structure of the SLM-produced CoCrFeMnNi alloy. This is because the rapid solidification of SLM contributes to dislocation accumulation and phase precipitation (Li R. et al., 2018). During the corrosion process, the formation and the distribution of the precipitates are factors affecting the surface activity (Barbucci et al., 1997). And the precipitates with high density were impressionable to the intergranular corrosion on the grain boundary (Huang et al., 2004). The significant increase of the grain boundaries and dislocation densities in microstructure also accelerate its corrosion. Hartley (1970) advocates that alloying elements preferentially migrate to grain boundary along with dislocation due to the established interaction energy gradient between alloying elements and dislocation. Meanwhile, due to the increased prevalence of diffusion pathways like dislocation or grain boundaries, alloying elements can easily interact with solution salt components to form more stable corrosion products (Maric et al., 2018). Therefore, due to the presence of high-density dislocation accumulation, dislocation entanglement, bending, and phase precipitation, SLM produced CoCrFeMnNi alloys are more vulnerable to corrosion.

Comparison of Different Planes From SLM Printed Samples

The corrosion behavior of different planes of SLM produced CoCrFeMnNi samples was also studied in this paper. As shown in **Figures 1**, **3**, the anti-corrosion property of the XY plane was better than that of the XZ plane. The result is attributed to the difference in the microstructure and phase in different planes. From **Figure 7**, cracks and holes in the XZ plane are larger and denser than those in the XY plane, and thus more effective surface areas contact the solution, which leads to a reduction in its corrosion performance. Other factors that can affect the corrosion property of CoCrFeMnNi alloy are grain boundary and grain orientation. In our previous study, equiaxed grains were obvious in the XY plane with the preference of <001<

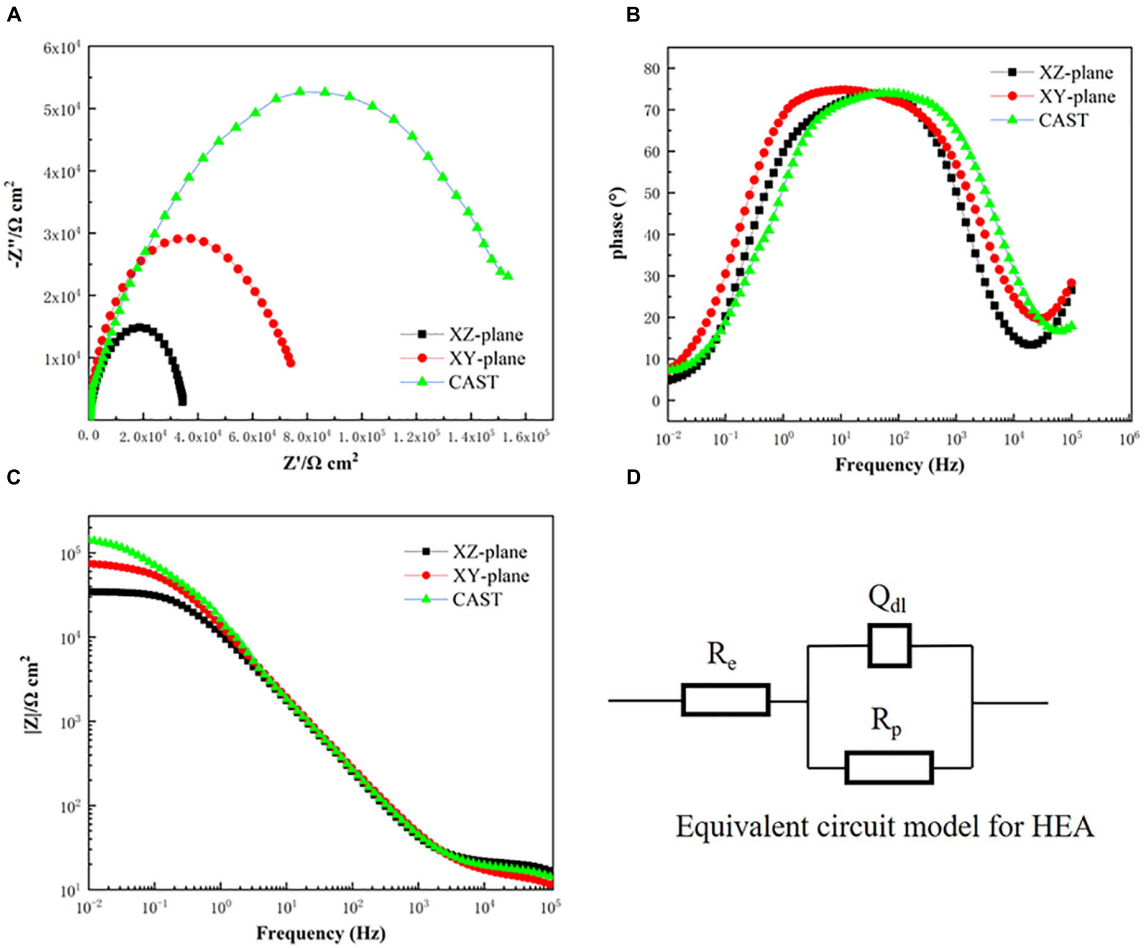

FIGURE 4 | The EIS results of the XY and XZ planes for the SLM printed HEA and casted HEA immersed in the aerated 3.5 wt.% NaCl solution at room temperature. **(A)** Nyquist plots, **(B,C)** Bode plots, **(D)** equivalent circuit model.

TABLE 2 | The fitting results of EIS of the XY and XZ planes for the SLM printed HEA and casted HEA in the aerated 3.5 wt.% NaCl solution at room temperature.

Samples	R_e (Ω cm^2)	Q_{dl}(Ω $^{-1}$cm^{-2} s^n)	n_{dl}	R_p (Ω cm^2)	Σ χ ^{2}
XZ-plane	16.03	1.72×10^{-5}	0.847	3.61×10^{4}	8.70×10^{-3}
XY-plane	16.05	1.54×10^{-5}	0.841	7.66×10^{4}	1.14×10^{-3}
Cast	16.09	1.21×10^{-7}	0.717	16.7×10^{4}	4.45×10^{-5}

and <101> orientations, while there is a mixed crystal structure biased toward columnar crystals with the aggregation of <001> orientations in the XZ plane (Li R. et al., 2018), which indicates that the grain size on the XY plane is smaller than that on the XZ plane. Lu et al. (Li, 2005) reported that the reduction of the grain size plays an important role in increasing electron activity near grain boundaries, which results in the reduction of the electron work function. Therefore, the surface of the XY plane is more reactive and tends to form a stable passivation film. Meanwhile, due to fewer surface defects, the passivation film formed on XY-plane is denser, as shown in **Figure 2**.

Generally, the competitive dissolution between grains with different atomic packing density on the surface induces greater effect than that of the grain boundary, which means that the effect of grain morphology on electrochemical dissolution is more effective than that of grain size (Li J. et al., 2018). And the effect of grain morphology in corrosion behavior is related to grain orientation. Theoretically, comparing the surface energy levels of the tightly and loosely arranged crystallographic could estimate the effect of grain orientation on the corrosion properties (Song et al., 2010). The tightly packed plane has higher atomic coordination and binding energy, while its surface energy and dissolution activation energy is lower (Jiang et al., 2017). The relationships between surface energy and corrosion rate of many materials have been studied (Song et al., 2010; Song and Xu, 2012). In our previous work, it has been found that

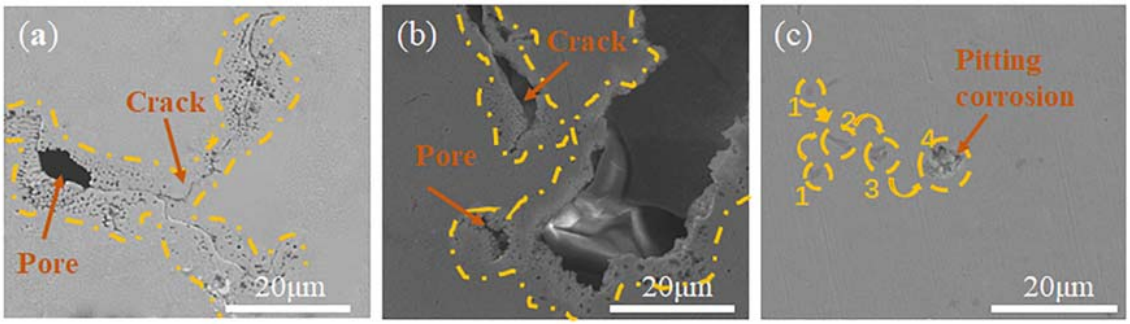

FIGURE 5 | SEM image of the Surface corrosion morphologies of samples with different planes of SLM produced CoCrFeMnNi and casted CoCrFeMnNi after electrochemical tests. **(a)** XZ plane; **(b)** XY plane; **(c)** casted CoCrFeMnNi.

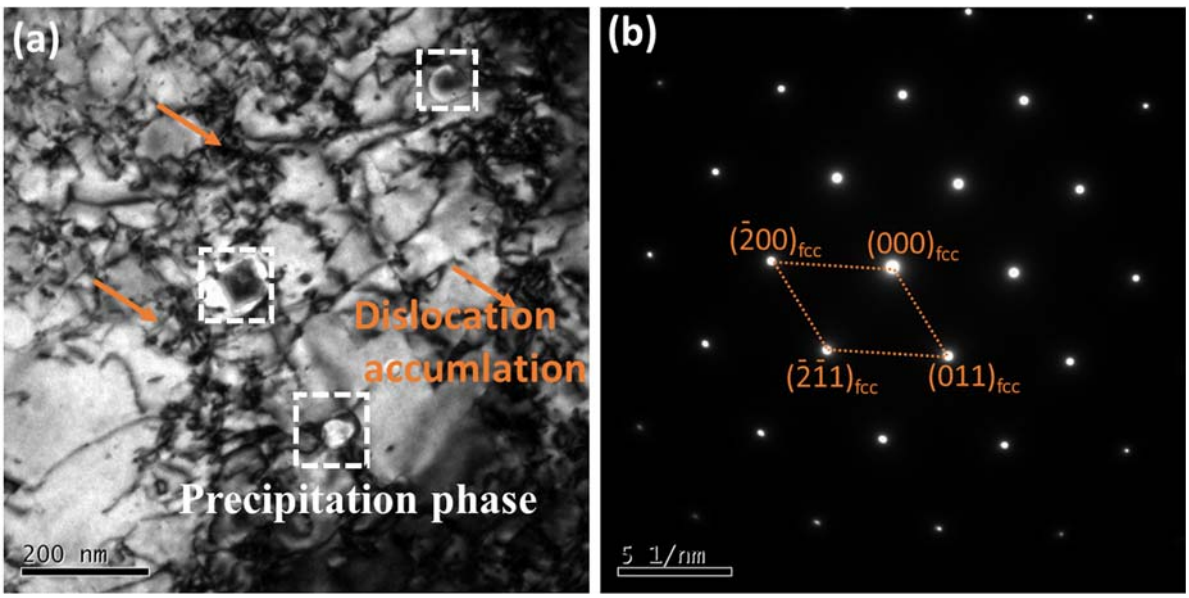

FIGURE 6 | Microstructure of the SLM processed CoCrFeMnNi HEA. **(a)** TEM bright field showing the high density of dislocation accumulation and dislocation network. **(b)** SAED pattern showing the primary FCC phase.

the SLM-produced CoCrFeMnNi has an FCC crystal structure (Li R. et al., 2018), which indicates that the atomic density in the (101) basal plane is higher than that in the (001) basal plane. This means that the surface energy in the (101) basal plane is higher than that in the (001) basal plane. Therefore, the corrosion property of the XZ plane was better than that of the XY plane in theory. These findings were contrary to the experimental results.

By contrast, effects of grain orientations on surface corrosion behavior of XY plane and XZ plane might not be significant. The SLM produced CoCrFeMnNi presents a similar lattice structure and lattice constant to austenitic iron in this study. Therefore, the data of austenitic steel could be used to understand the electrochemical dissolution properties of SLM-produced CoCrFeMnNi in different crystallographic planes. For the (001) and (101) basal planes of the austenitic iron, the surface energy was 2.133 and 2.255 J/m^2 for GGA-PW91 (Yu et al., 2009), respectively. The electrochemical anodic dissolution rate of the metal could be determined by the following equation (Kocijan et al., 2011):

$$I_a = nFke^{\left(Q + \alpha nFE/RT\right)} \tag{3}$$

where n is the number of electrons for the electrochemical process, k the reaction constants, F the Faraday constants, R the gas constants, Q the activation energy of metal ions escaping from the metal lattice and dissolving into solution, α the constant needed to replace activation energy with surface energy, E the electrode potential, and T the absolute temperature. The electrolyte solution has the same effect on Q and E of the surface of the crystallographic planes. In this study, due to the same experimental environment and equipment, we assumed that n and k are constant in different crystallographic planes.

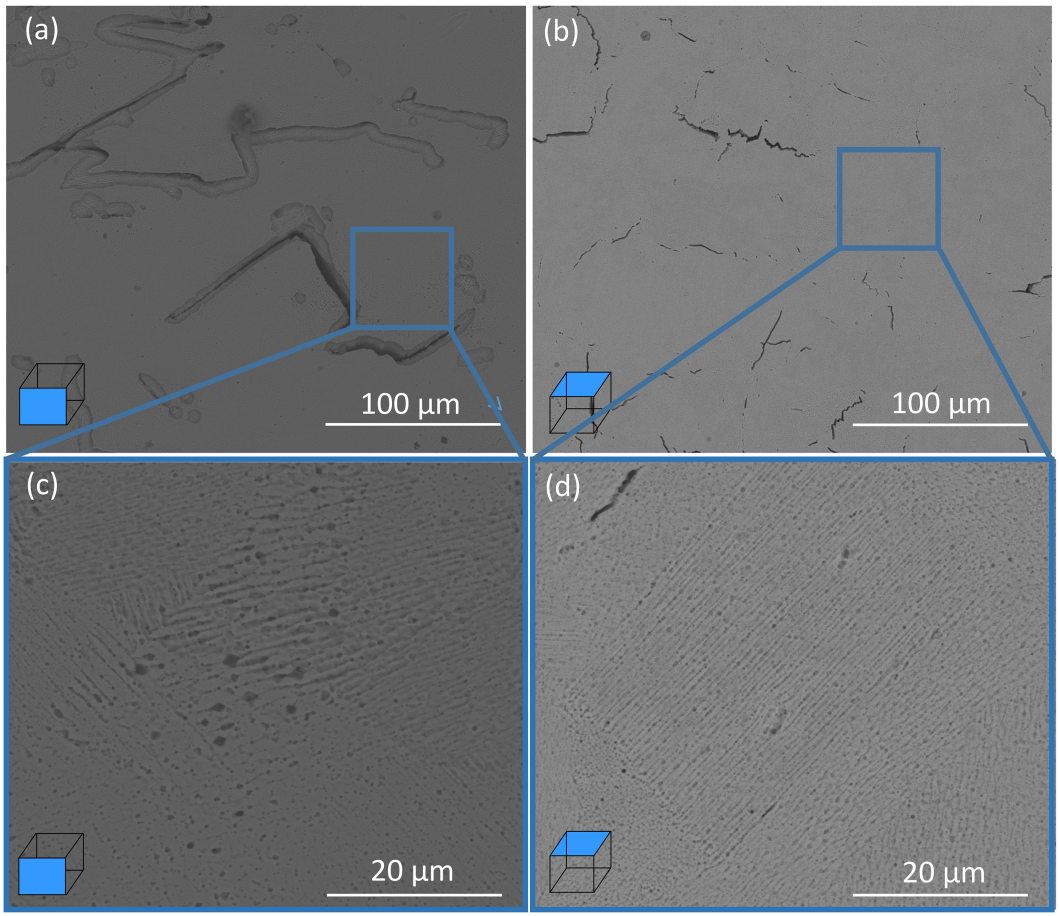

FIGURE 7 | SEM images of the SLM produced CoCrFeMnNi with the different planes. **(a)** XZ plane; **(b)** XY plane; **(c,d)** the characteristic morphologies of selection areas on XZ and XY planes, respectively.

At a given T at 25℃, the ratio of the anodic dissolution rate I_a^{XY-} of the XY plane over that I_a^{XZ-} of the XZ plane should be $\frac{I_a^{XY-}}{I_a^{XZ-}} = e^{\frac{\alpha\left(Q^{XY-}-Q^{XZ-}\right)}{RT}}$. If $\alpha = \frac{1}{2}$, after calculating surface energy values for austenite iron (001) and (101) theoretically, we obtain $\frac{I_a^{XY-}}{I_a^{XZ-}} = e^{\frac{\frac{1}{2}\times\left(\frac{1}{2}\times(2.133+2.225)-2.133\right)}{8.314\times298.13}} = 1.00001$, suggesting that electrochemical anodic dissolution rate of XY plane is slightly higher than that of the XZ plane in theory. Calculation results indicate that the competitive dissolution of grains with different atomic packing densities on the surface of CoCrFeMnNi prepared by SLM are not obvious. Corrosion resistance is mainly affected by surface morphology and grain boundaries in different planes of SLM-printed CoCrFeMnNi alloy.

CONCLUSION

This study focused on the comparison of corrosion behaviors between XY, XZ planes of SLM produced CoCrFeMnNi HEAs, and casted CoCrFeMnNi in the 3.5 wt.% NaCl solution. EIS and Tafel were used to study their electrochemical properties. Besides, SEM and TEM were used to analyze the surface morphology and crystal structure of the samples. Conclusions can be summarized as follows:

(1) Electrochemical tests show that the corrosion resistance of the casted CoCrFeMnNi is better than that of the SLM printed CoCrFeMnNi, and the corrosion resistance of the XY plane in SLM printed CoCrFeMnNi is better than that of its XZ plane.
(2) In the CoCrFeMnNi alloy prepared by SLM, a large number of structural defects increase the effective contact area with the solution. Dislocations facilitate the interaction of alloy elements with solution salt components and form more stable corrosion products. The precipitated phase causes partial areas to be preferentially corroded.
(3) In the CoCrFeMnNi prepared by SLM, cracks, and holes induces primary effects on the corrosion resistance. The cracks and holes in the XZ plane are larger and denser, which indicates that the XZ plane has a larger effective corrosion area during the corrosion process. And because of the small size of the XY plane grain, its surface reactivity

is higher and tends to form a stable passivation film. Electrochemical anodic dissolution rates of different planes were calculated, results show that the grain orientation has a slight influence on the corrosion properties of the XY and XZ planes, while surface morphology and grain boundary are two main factors which induce different corrosion performances.

DATA AVAILABILITY STATEMENT

All datasets presented in this study are included in the manuscript/supplementary material.

AUTHOR CONTRIBUTIONS

HP performed writing the original draft, conceptualization, and investigation. ZL performed the resources and supervision. PN performed the resources and investigation. ZZ performed the investigation. RL performed writing, reviewing and editing, and supervision. All authors contributed to the article and approved the submitted version.

FUNDING

This work was financially supported by National Key R&D Program of China (2017YFB0306305), Science and Technology Plan Project of Shenzhen (JCYJ20180508151903646), and Huxiang Young Talents (2018RS3007).

ACKNOWLEDGMENTS

The authors wish to acknowledge the National Natural Science Foundation of China (51505166 and 51871249).

REFERENCES

Barbucci, A., Cerisola, G., Bruzzone, G., and Saccone, A. (1997). Activation of aluminium anodes by the presence of intermetallic compounds. *Electrochim. Acta* 42, 2369–2380. doi: 10.1016/S0013-4686(96)00420-3

Brandl, E., Heckenberger, U., Holzinger, V., and Buchbinder, D. (2012). Additive manufactured AlSi10Mg samples using selective laser melting (SLM): microstructure, high cycle fatigue, and fracture behavior. *Mater. Des.* 34, 159–169. doi: 10.1016/j.matdes.2011.07.067

Chen, H., Gu, D., Xiong, J., and Xia, M. (2017). Improving additive manufacturing processability of hard-to-process overhanging structure by selective laser melting. *J. Mater. Process. Technol.* 250, 99–108. doi: 10.1016/j.jmatprotec.2017.06.044

Chen, Y., Zhang, J., Gu, X., Dai, N., Qin, P., and Zhang, L. C. (2018). Distinction of corrosion resistance of selective laser melted Al-12Si alloy on different planes. *J. Alloys Compd.* 747, 648–658. doi: 10.1016/j.jallcom.2018.03.062

Della Rovere, C. A., Alano, J. H., Silva, R., Nascente, P. A. P., Otubo, J., and Kuri, S. E. (2012). Characterization of passive films on shape memory stainless steels. *Corros. Sci.* 57, 154–161. doi: 10.1016/j.corsci.2011.12.022

Dong, K., Song, Y., Shan, D., and Han, E. H. (2015). Corrosion behavior of a self-sealing pore micro-arc oxidation film on AM60 magnesium alloy. *Corros. Sci.* 100, 275–283. doi: 10.1016/j.corsci.2015.08.004

Fajardo, S., Bastidas, D. M., Criado, M., and Bastidas, J. M. (2014). Electrochemical study on the corrosion behaviour of a new low-nickel stainless steel in carbonated alkaline solution in the presence of chlorides. *Electrochim. Acta* 129, 160–170. doi: 10.1016/j.electacta.2014.02.107

Fan, X., Wang, Y., Zou, B., Gu, L., Huang, W., and Cao, X. (2013). Preparation and corrosion resistance of MAO/Ni-P composite coat on Mg alloy. *Appl. Surf. Sci.* 277, 272–280. doi: 10.1016/j.apsusc.2013.04.044

Fazakas, É, Wang, J. Q., Zadorozhnyy, V., Louzguine-Luzgin, D. V., and Varga, L. K. (2014). Microstructural evolution and corrosion behavior of Al25Ti 25Ga25Be25 equi-molar composition alloy. *Mater. Corros* 65, 691–695. doi: 10.1002/maco.201206941

Gan, Z. H., Xu, L. M., Lu, Z. H., Zhou, H. H., Song, C. H., and Huang, F. (2013). A novel high-entropy alloy AlMgZnSnPbCuMnNi with low free corrosion potential. *Appl. Mech. Mater.* 327, 103–107. doi: 10.4028/www.scientific.net/AMM.327.103

Gu, Y., Chen, C. F., Bandopadhyay, S., Ning, C., Zhang, Y., and Guo, Y. (2012). Corrosion mechanism and model of pulsed DC microarc oxidation treated AZ31 alloy in simulated body fluid. *Appl. Surf. Sci.* 258, 6116–6126. doi: 10.1016/j.apsusc.2012.03.016

Guo, H. X., Ma, Y., Wang, J. S., Wang, Y. S., Dong, H. R., and Hao, Y. (2012). Corrosion behavior of micro-arc oxidation coating on AZ91D magnesium alloy in NaCl solutions with different concentrations. *Trans. Nonferrous Met. Soc. China* 22, 1786–1793. doi: 10.1016/S1003-6326(11)61388-5

Hartley, C. S. (1970). Kinetics of solute atom drift to dislocation dipoles. *Acta Metall.* 18, 271–273. doi: 10.1016/0001-6160(70)90034-9

Hsu, Y. J., Chiang, W. C., and Wu, J. K. (2005). Corrosion behavior of FeCoNiCrCux high-entropy alloys in 3.5% sodium chloride solution. *Mater. Chem. Phys.* 92, 1–290. doi: 10.1016/j.matchemphys.2005.01.001

Huang, Y. S., Zeng, X. T., Hu, X. F., and Liu, F. M. (2004). Corrosion resistance properties of electroless nickel composite coatings. *Electrochim. Acta* 49, 4313–4319. doi: 10.1016/j.electacta.2004.04.023

Jiang, B., Xiang, Q., Atrens, A., Song, J., and Pan, F. (2017). Influence of crystallographic texture and grain size on the corrosion behaviour of as-extruded Mg alloy AZ31 sheets. *Corros. Sci.* 126, 374–380. doi: 10.1016/j.corsci.2017.08.004

Joseph, J., Stanford, N., Hodgson, P., and Fabijanic, D. M. (2017). Tension/compression asymmetry in additive manufactured face centered cubic high entropy alloy. *Scr. Mater.* 129, 30–34. doi: 10.1016/j.scriptamat.2016.10.023

Kocijan, A., Merl, D. K., and Jenko, M. (2011). The corrosion behaviour of austenitic and duplex stainless steels in artificial saliva with the addition of fluoride. *Corros. Sci.* 53, 776–783. doi: 10.1016/j.corsci.2010.11.010

Kong, D., Dong, C., Ni, X., Zhang, L., Yao, J., Man, C., et al. (2019). Mechanical properties and corrosion behavior of selective laser melted 316L stainless steel after different heat treatment processes. *J. Mater. Sci. Technol.* 35, 1499–1507. doi: 10.1016/j.jmst.2019.03.003

Kumar, N., Fusco, M., Komarasamy, M., Mishra, R. S., Bourham, M., and Murty, K. L. (2017). Understanding effect of 3.5 wt.% NaCl on the corrosion of Al0.1CoCrFeNi high-entropy alloy. *J. Nucl. Mater.* 495, 154–163. doi: 10.1016/j.jnucmat.2017.08.015

Li, J., Lin, X., Guo, P., Song, M., and Huang, W. (2018). Electrochemical behaviour of laser solid formed Ti–6Al–4V alloy in a highly concentrated NaCl solution. *Corros. Sci.* 142, 161–174. doi: 10.1016/j.corsci.2018.07.023

Li, L., Li, R., Yuan, T., Chen, C., Zhang, Z., and Li, X. (2020). Microstructures and tensile properties of a selective laser melted Al–Zn–Mg–Cu (Al7075) alloy by Si and Zr microalloying. *Mater. Sci. Eng. A* 787:139492. doi: 10.1016/j.msea.2020.139492

Li, R., Niu, P., Yuan, T., Cao, P., Chen, C., and Zhou, K. (2018). Selective laser melting of an equiatomic CoCrFeMnNi high-entropy alloy: processability, non-equilibrium microstructure and mechanical property. *J. Alloys Compd.* 746, 125–134. doi: 10.1016/j.jallcom.2018.02.298

Li, R., Wang, M., Li, Z., Cao, P., Yuan, T., and Zhu, H. (2020). Developing a high-strength Al-Mg-Si-Sc-Zr alloy for selective laser melting: crack-inhibiting and multiple strengthening mechanisms. *Acta Mater.* 193, 83–98. doi: 10.1016/j.actamat.2020.03.060

Li, D. Y. (2005). Electron work function at grain boundary and the corrosion behavior of nanocrystalline metallic materials. *MRS Proc.* 887, 227–235. doi: 10.1557/proc-0887-q05-03

Liu, F., Shan, D., Song, Y., and Han, E. H. (2011). Effect of additives on the properties of plasma electrolytic oxidation coatings formed on AM50 magnesium alloy in electrolytes containing K2ZrF6. *Surf. Coatings Technol.* 206, 455–463. doi: 10.1016/j.surfcoat.2011.07.054

Luo, H., Li, Z., Mingers, A. M., and Raabe, D. (2018). Corrosion behavior of an equiatomic CoCrFeMnNi high-entropy alloy compared with 304 stainless steel in sulfuric acid solution. *Corros. Sci.* 134, 131–139. doi: 10.1016/j.corsci.2018.02.031

Maric, M., Muránsky, O., Karatchevtseva, I., Ungár, T., Hester, J., Studer, A., et al. (2018). The effect of cold-rolling on the microstructure and corrosion behaviour of 316L alloy in FLiNaK molten salt. *Corros. Sci.* 142, 133–144. doi: 10.1016/j.corsci.2018.07.006

Montero Sistiaga, M. L., Mertens, R., Vrancken, B., Wang, X., Van Hooreweder, B., Kruth, J. P., et al. (2016). Changing the alloy composition of Al7075 for better processability by selective laser melting. *J. Mater. Process. Technol.* 238, 437–445. doi: 10.1016/j.jmatprotec.2016.08.003

Niu, P., Li, R., Zhu, S., Wang, M., Chen, C., and Yuan, T. (2020). Hot cracking, crystal orientation and compressive strength of an equimolar CoCrFeMnNi high-entropy alloy printed by selective laser melting. *Opt. Laser Technol.* 127:106147. doi: 10.1016/j.optlastec.2020.106147

Niu, P. D., Li, R. D., Yuan, T. C., Zhu, S. Y., Chen, C., Wang, M. B., et al. (2019). Microstructures and properties of an equimolar AlCoCrFeNi high entropy alloy printed by selective laser melting. *Intermetallics* 104, 24–32. doi: 10.1016/j.intermet.2018.10.018

Pan, Y. K., Chen, C. Z., Wang, D. G., and Zhao, T. G. (2013). Effects of phosphates on microstructure and bioactivity of micro-arc oxidized calcium phosphate coatings on Mg-Zn-Zr magnesium alloy. *Colloids Surfaces B Biointerfaces* 109, 1–9. doi: 10.1016/j.colsurfb.2013.03.026

Qiu, X. W., Zhang, Y. P., He, L., and Liu, C. G. (2013). Microstructure and corrosion resistance of AlCrFeCuCo high entropy alloy. *J. Alloys Compd.* 549, 195–199. doi: 10.1016/j.jallcom.2012.09.091

Qiu, Y., Thomas, S., Fabijanic, D., Barlow, A. J., Fraser, H. L., and Birbilis, N. (2019). Microstructural evolution, electrochemical and corrosion properties of Al x CoCrFeNiTi y high entropy alloys. *Mater. Des.* 170, 1–15. doi: 10.1016/j.matdes.2019.107698

Ren, B., Liu, Z. X., Li, D. M., Shi, L., Cai, B., and Wang, M. X. (2012). Corrosion behavior of CuCrFeNiMn high entropy alloy system in 1 M sulfuric acid solution. *Mater. Corros.* 63, 828–834. doi: 10.1002/maco.201106072

Shang, W., Chen, B., Shi, X., Chen, Y., and Xiao, X. (2009). Electrochemical corrosion behavior of composite MAO/sol-gel coatings on magnesium alloy AZ91D using combined micro-arc oxidation and sol-gel technique. *J. Alloys Compd.* 474, 541–545. doi: 10.1016/j.jallcom.2008.06.135

Song, G. L., Mishra, R., and Xu, Z. (2010). Crystallographic orientation and electrochemical activity of AZ31 Mg alloy. *Electrochem. Commun.* 12, 1009–1012. doi: 10.1016/j.elecom.2010.05.011

Song, G. L., and Xu, Z. (2012). Crystal orientation and electrochemical corrosion of polycrystalline Mg. *Corros. Sci.* 63, 100–112. doi: 10.1016/j.corsci.2012.05.019

Wang, M. J., Li, C. F., and Yen, S. K. (2013). Electrolytic MgO/ZrO2 duplex-layer coating on AZ91D magnesium alloy for corrosion resistance. *Corros. Sci.* 76, 142–153. doi: 10.1016/j.corsci.2013.06.037

Wysocki, B., Maj, P., Krawczyńska, A., Rożniatowski, K., Zdunek, J., Kurzydłowski, K. J., et al. (2017). Microstructure and mechanical properties investigation of CP titanium processed by selective laser melting (SLM). *J. Mater. Process. Technol.* 241, 13–23. doi: 10.1016/j.jmatprotec.2016.10.022

Yao, Z., Xu, Y., Liu, Y., Wang, D., Jiang, Z., and Wang, F. (2011). Structure and corrosion resistance of ZrO2 ceramic coatings on AZ91D Mg alloys by plasma electrolytic oxidation. *J. Alloys Compd.* 509, 8469–8474. doi: 10.1016/j.jallcom.2011.06.011

Ye, Y. F., Wang, Q., Lu, J., Liu, C. T., and Yang, Y. (2016). High-entropy alloy: challenges and prospects. *Mater. Today* 19, 349–362. doi: 10.1016/j.mattod.2015.11.026

Yu, J., Lin, X., Wang, J., Chen, J., and Huang, W. (2009). First-principles study of the relaxation and energy of bcc-Fe, fcc-Fe and AISI-304 stainless steel surfaces. *Appl. Surf. Sci.* 255, 9032–9039. doi: 10.1016/j.apsusc.2009.06.087

Zhang, H., Gu, D., Xi, L., Zhang, H., Xia, M., and Ma, C. (2019). Anisotropic corrosion resistance of TiC reinforced Ni-based composites fabricated by selective laser melting. *J. Mater. Sci. Technol.* 35, 1128–1136. doi: 10.1016/j.jmst.2018.12.020

Zhang, H., Xu, W., Xu, Y., Lu, Z., and Li, D. (2018). The thermal-mechanical behavior of WTaMoNb high-entropy alloy via selective laser melting (SLM): experiment and simulation. *Int. J. Adv. Manuf. Technol.* 96, 461–474. doi: 10.1007/s00170-017-1331-9

Zhang, Y., Chen, B., and Guo, Z. (2014a). Electrochemical properties and microstructure of Al/Pb-Ag and Al/Pb-Ag-Co anodes for zinc electrowinning. *Acta Metall. Sin.* 27, 331–337. doi: 10.1007/s40195-014-0050-6

Zhang, Y., Zuo, T. T., Tang, Z., Gao, M. C., Dahmen, K. A., Liaw, P. K., et al. (2014b). Microstructures and properties of high-entropy alloys. *Prog. Mater. Sci.* 61, 1–93. doi: 10.1016/j.pmatsci.2013.10.001

Ziomek.-Moroz, M., Alvaro Rodriguez, M., and Joseph Tylczak, H. (2017). Plays a dominant role on the total mixing entropy, and can be calculated using Equation 1 for ideal and regular solutions. This equation represents a good approximation for liquid alloys and many solid alloys close to melting temperature. *X, ECS Trans.* 77, 741–752.

Conflict of Interest: The authors declare that the research was conducted in the absence of any commercial or financial relationships that could be construed as a potential conflict of interest.